Predicting the effect of droplet geometry and size distribution on atmospheric corrosion

Van den Steen, N.; Gonzalez-Garcia, Y.; Mol, J. M.C.; Terryn, H.; Van Ingelgem, Y.

DOI
10.1016/j.corsci.2022.110308

Publication date
2022

Document Version
Final published version

Published in
Corrosion Science

Corrosion Science 202 (2022) 110308

Contents lists available at ScienceDirect

Corrosion Science

journal homepage: www.elsevier.com/locate/corsci

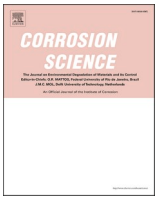

Predicting the effect of droplet geometry and size distribution on atmospheric corrosion

N. Van den Steen [a,*], Y. Gonzalez-Garcia [b], J.M.C. Mol [b], H. Terryn [a], Y. Van Ingelgem [a]

[a] Research Group Electrochemical and Surface Engineering, Vrije Universiteit Brussel, Pleinlaan 2, 1050 Brussels, Belgium
[b] Delft University of Technology, Department of Materials Science and Engineering, Mekelweg 2, 2628 CD Delft, The Netherlands

ARTICLE INFO

Keywords:
Atmospheric corrosion
Modelling
Size distribution
Droplet geometry
Droplet size distribution

ABSTRACT

A new approach is proposed to numerically predict and study atmospheric corrosion for ranging droplet size distributions and the influence of the droplet geometry. The proposed methodology allows for a corrosion prediction based on observed droplet size distributions and droplet contact angles. A mechanistic finite element model, including oxygen transport and Butler-Volmer kinetics, is solved in order to obtain the current density as a function of the droplet geometry. This is done for a range of both droplet radii and contact angles. The computed corrosion current densities are then used as input for imposed droplet size distributions. This allows for a calculated material loss estimation for different distributions and electrolyte configurations and shows the extent of the impact of the droplet size distribution on atmospheric corrosion.

1. Introduction

Atmospheric corrosion is a highly complex phenomenon, acting over relatively long time scales. When studying atmospheric corrosion, it is very hard to link observed corrosion products and losses to possible mechanisms and phenomena. Initial corrosion mechanisms and kinetics (first hours/days) might for example differ strongly from those dominating in the long term.

To overcome the long timescales over which atmospheric corrosion acts, accelerated corrosion tests are employed to allow early assessment of the corrosion resistance of metals and effectiveness of protective coatings. These accelerated corrosion tests partially solve the time constraints but give rise to new problems. A first hurdle is the lack of a clear correlation between the results of an accelerated corrosion test and the real outdoor corrosion resistance [1–5]. Not only the lack of this correlation is a problem, but also the corrosion protection performance evaluation is strongly depended on the selected standard [6].

Even for an accelerated test, described through standards, there are still a lot of unknowns. Due to the dynamic nature of the electrolyte, corrosion products and environmental conditions, a full description over time of all the processes is difficult to construct. The electrolyte behaviour (composition, geometry, distribution, etc.) for example, is currently not fully monitored nor completely understood. The electrolyte volume, composition and geometry play a key factor in atmospheric corrosion. This was already established by Stratmann et al. in 1990 [7]. In recent years, electrolyte formation and geometry is attracting more attention, both experimentally [8–11] and numerically [12–15]. Weissenrieder et al. [8] studied filiform corrosion under droplets by depositing small amounts of NaCl and controlling the relative humidity and thus controlling the droplet size. Liu et al. [9] used a beam electrode setup to examine corrosion under thin seawater layers. With the used setup, the electrolyte layer thickness and thus the accessibility to oxygen, can be controlled. However, still a large volume of electrolyte is in contact with the electrodes, which has an impact on species concentrations. Both Ahn et al. [10] and Wan et al. [11] equipped samples with corrosion monitoring sensors during cyclic testing. The key difference between both is that the setup of Wan et al. allows for the measurement of both the corrosion current and the electrolyte thickness, while the setup of Ahn et al. is limited to the corrosion currents. In a study done by LeBozec [6], significant differences between identical tests performed in different laboratories or climate chambers were observed. The electrolyte thickness as a result of condensation, is strongly related to the surface temperature of the sample. Cole et al. [12] therefore constructed a mathematical model to predict the surface temperature based on the environmental conditions. Van den Steen et al. [13,14] built a model which predicts the electrolyte thickness evolution

* Corresponding author.
E-mail addresses: nils.van.den.steen@vub.be (N. Van den Steen), y.gonzalezgarcia@tudelft.nl (Y. Gonzalez-Garcia), J.M.C.Mol@tudelft.nl (J.M.C. Mol), herman.terryn@vub.be (H. Terryn), yves.van.ingelgem@vub.be (Y. Van Ingelgem).

https://doi.org/10.1016/j.corsci.2022.110308
Received 11 October 2021; Received in revised form 25 March 2022; Accepted 6 April 2022
Available online 14 April 2022

based on material properties and the environmental conditions. Combined with a corrosion model, this approach allows for a corrosion loss prediction during accelerated corrosion tests. Parker et al. [16] showed that a high degree of relative humidity control - and thus indirect electrolyte thickness control - during an accelerated corrosion tests is important in order to be able to reproduce results using different climate chambers. Katona et al. [15] provides a detailed study of the different transport behaviour in a thick film. Chen et al. [17] developed a model to predict the number and connectivity of droplets inside a coating defect during a neutral salt spray test. In this model, the droplet generation, growth and transport was predicted. From this predicted state, the inhibitor concentration in the interconnected droplets inside a coating defect was calculated based on a fixed release rate. The inhibitor concentrations, combined with the inhibitor efficiency, enable the authors to estimate the daily pit increments.

Experimental investigations further demonstrate the high complex nature of the problem, with corrosion rates depending on local current and past conditions. Cole et al. examined the link between the wetting behaviour of a surface and observed corrosion [18]. In a second paper, now focused on modelling, Cole et al. emphasised that a detailed knowledge of the present salts, their phases and binding with the surface are critical, as this will determine the quantity (volume) and corrosivity of the electrolyte [19]. In the final part of the paper series [20], Cole et al. developed a framework for the prediction of salt retention on a surface. In this work generalised rules are proposed for salt removal. The theoretically found minimal required amount of rain showed good agreement with experimental findings. Also for galvanic corrosion, the importance of droplets was demonstrated in literature [21]. Tsuru et al. [22] approached the problem from the opposite direction and studied how the corrosion itself influences or even dictates the contact angle, droplet retention, …of the droplets. Similar research was performed by El-Mahdy [23] on carbon steel and by Misyura et al. [24] on aluminium. Azmat et al. [25] examined the heterogeneous composition and effect of acidification of the electrolyte on the corrosion products and morphology on zinc. A more electrochemically oriented study on zinc was performed by Muster et al. [26]. They used a multi-electrode to examine differences between advancing and receding droplets and the size dependent effects of the electrolyte composition. Wang et al. [27] applied a similar approach on steel substrates, including time evolution. In this work, Wang reports that corrosion increases with increasing droplet size. This statement is in direct contradiction with the work of Li et al. [28], but was confirmed by Tang et al. [29] using a three-electrode array. The latter used micro-capillaries to study marine corrosion in high humidity. Related to the humidity, Schindelholz et al. [30] studied the minimal relative humidity needed for the onset of corrosion. In this work, it is reported that corrosion can already occur at a relative humidity as low as 33% in the presence of NaCl particles.

Venkatraman et al. implemented a single droplet model [31,32]. In these works, steady-state conditions are assumed. This means that there is no corrosion product build-up or any change in the droplet geometry. This work forms the basis of the single droplet modelling in this work. An extensive overview of droplet corrosion modelling can be found in [33].

A droplet size distribution is dependent on the material (substrate, oxide), roughness, electrolyte composition, deposition rate and deposition type, among others [34,35]. It is thus clear that this is a complex, interdisciplinary problem. The primary goal of this work is to present a new modelling approach, which allows us to asses the corrosion impact of different droplet size distributions and can be seen as the next step into a better understanding of atmospheric corrosion. The differences in (dropwise) electrolyte (quantity, shape, distribution) between different accelerated corrosion tests and identical tests in different cabinets, could be the key parameter to explain the observed differences in corrosion behaviour. Furthermore, a correlation between accelerated tests and outdoor exposure tests could be found, resulting in better interpretation of experimental results and improved test standards. With this the authors aim to raise the attention of the atmospheric corrosion science community and to efficiently steer experimental research in the field of well-controlled and small electrolyte droplet volumes.

2. Approach

First of all, the problem of corrosion resulting from multiple droplets on a surface at a specific size distribution was split into two parts: (i) the corrosion caused by a single droplet and (ii) the corrosion resulting from multiple droplets with varying sizes and geometries (contact angle). In this work, a droplet distribution refers to a collection of droplets with varying sizes, according to a given distribution. In the presented approach, the droplet size distributions are assumed to be available from either experimental measurements or numerical calculations. Furthermore, the approach does not make any assumptions about the origin of the droplets. This means that the approach could be applied for both directly deposited droplets (spray, printed with inkjet, ...) or dropwise condensation. The contact angle of the droplets is assumed to be constant and identical for all droplets. In the first section, the single droplet modelling will be discussed. This is a finite element model which predicts the (area) average corrosion rate for stationary conditions depending on the geometry of the droplet and the electrolyte composition and electrode/sample material. The impact of the different included geometrical parameters will be evaluated here on the single droplet level. The second section covers the more realistic situation: multiple droplets on a surface at a certain size distribution. The corrosion rates will be compared for different size distributions and droplet contact angles. The single droplet model was implemented in COMSOL Multiphysics. While for the calculations involving droplet distributions were implemented in Python.

2.1. Single droplet model

As previously indicated, the work of Venkatraman et al. forms the basis of the single droplet model applied in this work [31,32]. For the purpose of this work, the implemented physics are kept limited and only the oxygen transport is considered. The implemented model is almost identical to the description given in [31], apart from the included species. In order to keep the initial model simple, the metal ions were not considered. The biggest addition in this work, is that not the saturated oxygen concentration is imposed at the air-electrolyte interface, but a concentration dependent flux. With this improvement, the oxygen uptake rate is limited when compared to imposing a constant saturated concentration on this boundary. When imposing a fixed concentration on the boundary, the (inward) oxygen flux is unlimited and hence for small droplets or close to the edge of a droplet unrealistically high fluxes would be imposed.

2.1.1. Electrochemistry

Two electrode reactions are implemented on the same electrode surface. The parameter values are extracted from Venkatraman et al. [32]. The first electrode reaction is the (two-electron) oxygen reduction reaction, implemented through the Butler-Volmer equation describing the local current density (i_{loc}) given by

$$i_{loc}^{\mathrm{ORR}} = i_{0,\mathrm{ORR}}\left(-\frac{c_{O_2}}{c_{0,O_2}} \exp\left(\frac{-n_{\mathrm{ORR}}\alpha_c F\eta}{RT}\right)\right) \tag{1}$$

for which $i_{0,\mathrm{ORR}}$ is the oxygen reduction exchange current density, c_{O_2} is the oxygen concentration, c_{0,O_2} is the saturated oxygen concentration, n_{ORR} is the number of involved electrons and α_c the cathodic transfer coefficient.

η is the overpotential given by

$$\eta = \phi_{s,ext} - \phi_l - E_{eq}, \tag{2}$$

with $\phi_{s,ext}$ the external electrode potential, ϕ_l the electrolyte

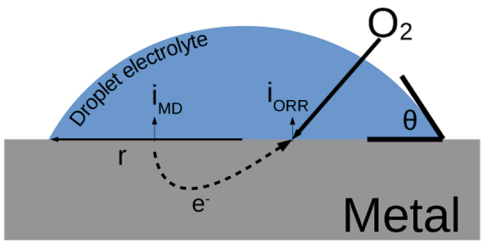

Fig. 1. Illustration of the oxygen reduction and metal dissolution current densities in a droplet with r the droplet radius, θ the contact angle, i^{MD} and i^{ORR} the metal dissolution and oxygen reduction current densities, respectively.

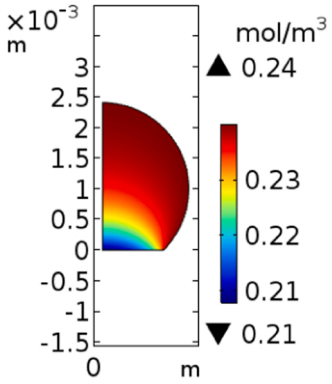

Fig. 2. Axisymmetric geometry of a droplet used in this work. The colorscale indicates the steady-state oxygen concentration (mol/m^3) resulting on iron in a droplet with a radius of 1 mm and a contact angle of 135°.

potential and E_{eq} the equilibrium potential.

Venkatraman et al. states in his work that a direct 4-electron pathway is competing with an indirect pathway. In the indirect pathway, each partial step involves 2 electrons. In a typical system, it is either the 2- or 4-electron pathway. When only considering the kinetics, and not the reaction products, the model implementation for the 2-electron pathway and 4-electron pathway is identical. For all shown results in Venkatraman's work, the 2-electron pathway was followed. Therefore, the 2-electron pathway was used in this work.

The metal dissolution current density (i_{loc}^{MD}) is given by

$$i_{loc}^{MD} = i_{0,MD}\left(\exp\left(\frac{n_{MD}\alpha_a F\eta}{RT}\right)\right). \tag{3}$$

The corrosion current density is thus given by

$$i^{MD} = -i^{ORR} = i_{corr}. \tag{4}$$

The system is illustrated in Fig. 1 with r the droplet radius, θ the contact angle, i^{MD} and i^{ORR} the metal dissolution and oxygen reduction current densities, respectively.

2.1.2. Mass transport

In this model, the only modelled species is the oxygen. The transport of the oxygen is modelled as a pure diffusion phenomenon [14]. At the electrode-electrolyte interface, a sink (consumption of the species) is implemented linked with the oxygen reduction reaction. On the exterior, curved boundary, an inward flux is imposed depending on the local and saturated oxygen concentration. The imposed flux is written as

$$N_{0,c} = K_{O_2}\cdot\left(1 - \frac{c_{O_2}}{c_{0,O_2}}\right), \tag{5}$$

with K_{O_2} the oxygen uptake rate ($k_{O_2} = 3.5e^{-5} mol \quad m^{-2}s^{-1}$) given by [36], c_{O_2} the local oxygen concentration and c_{0,O_2} the saturated oxygen concentration. In the current model, the temperature is assumed to be constant and equal to 25 °C.

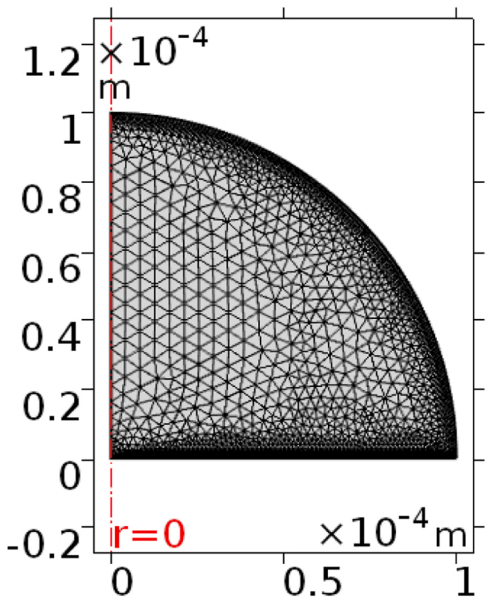

Fig. 3. The mesh for a single droplet simulation.

2.1.3. Geometry

The model uses an axisymmetric geometry around the vertical axis as illustrated in Fig. 2. Asymmetrical droplets, for example due to gravity on an inclined surface, would only change the geometry and not the model itself, but they are not considered in this work.

The geometry in this work is a function of the contact angle and the droplet (contact) radius. The effect of both of these parameters will be evaluated in this work.

The mesh is illustrated in Fig. 3 and is chosen so that a further mesh refinement does not alter the results. The maximal size of the elements is set to $5.3e^{-6}$ m and minimal $3.e^{-8}$ m. The electrolyte/electrode interface consists of at least 100 elements, while the electrolyte/air interface has at least 150 elements. This results in 3710 domain and 328 boundary elements for a droplet with a radius of 1 mm and a contact angle of 90°.

2.2. Droplet size distribution

Droplets can form through condensation or direct deposition. Four stages of growth can be identified [37] on horizontal surfaces illustrated in Fig. 4.

a) Initially the surface coverage is low, with almost no coalescence taking place. During this stage, the droplets will be very small and the impact on the total corrosion can probably be assumed minimal.
b) In the next stage, the droplets grow and coalesce without new droplets appearing on the newly created bare surface between the droplets. During this stage, the droplets sizes are close to uniformity.
c) During the third stage, the cleared areas form new nucleation sites for new (small) droplets.
d) In the long-term stage, droplets of all sizes are present on the surface, forming a steady-state dropwise condensation regime.

2.2.1. Experimental data (literature)

To the best of our knowledge, the state of the electrolyte within accelerated corrosion test experiments (distribution, geometry, etc.) is rarely reported in literature. This can be attributed to the intended goal of these tests in most applications. In the work of LeBozec et al. [3] the performance of different accelerated corrosion tests are compared with

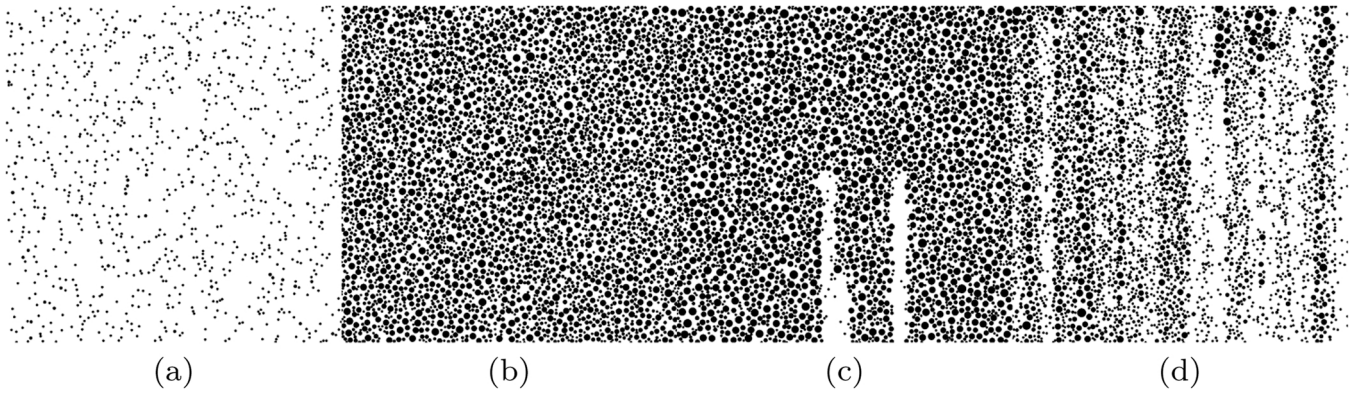

Fig. 4. Illustrations of the four different stages of droplet formation: a) Low surface coverage with almost no coalescence; b) Second stage with mostly coalescence; c) Start of runoff; d) Steady-state regime.

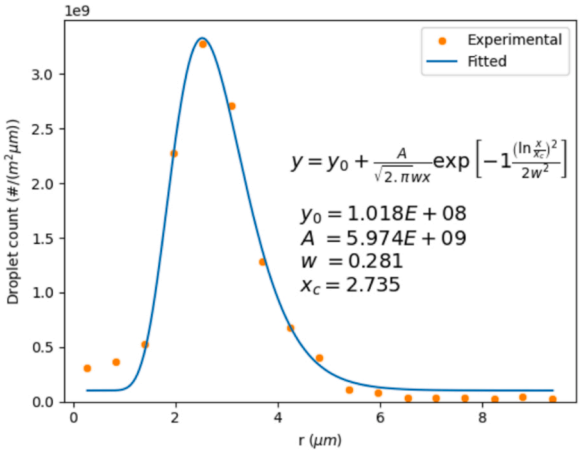

Fig. 5. Droplet distribution and lognormal fitting based on data measured by Song et al. [38] after 20 s of saturated vapour deposition in an environment with a temperature of 25.9 ˚C, a humidity between 75% and 80%, a surface subcooling of about 5.5 K and a measured contact angle around 110.8˚.

each other and with outdoor exposure tests. The goal is not to determine how the corrosion progresses, but only how the coatings and the accelerated tests perform. It is thus difficult to obtain relevant droplet size distributions for outdoor exposure or accelerated corrosion tests.

In this work, no experimental data was gathered and only data from literature was used. To evaluate the effect of different distributions, the size distribution taken from literature was shifted to bigger radii (the average droplet radius was increased by 5, 7.5, 10 and 20 μm).

To the best of our knowledge, no experimental size distributions are determined within the frame of prior corrosion research. For an initial evaluation, data obtained by Song et al. [38] was used and is illustrated below (Fig. 5). The illustrated droplet size distribution was obtained by Song et al. [38] after 20 s of saturated vapour deposition in an environment with a temperature of 25.9 ˚C, a humidity between 75% and 80%, a polished, copper surface subcooled by about 5.5 K and a measured contact angle around 110.8˚. Such amount of subcooling in a humid environment would for example be feasible during night-time cooling during a clear night.

2.2.2. Distribution shift and constraints/fitting

A given distribution illustrated in Fig. 6a can be shifted to different average radii in a couple of different ways. This can be accomplished while (i) keeping the total number of droplets, (ii) the covered area fraction, or (iii) the total electrolyte volume constant. These different distribution shifts are illustrated in Fig. 6, starting from the reference distribution illustrated in Fig. 6a. To assess the impact of the average droplet size of a distribution, all distribution parameters are kept constant. In reality, the distribution can look completely different when the average droplet size increases. How these distribution parameters change will strongly depend on the type of deposition (origin) of the droplets and falls outside the scope of this work. The blue circles illustrate the original droplets, while the orange circles illustrate the droplets of the shifted distribution. These types of shifts are a theoretical exercise and will only be encountered in specific conditions. An approximately constant volume could possibly be encountered on a samples during a salt spray (fog) with different nozzles but identical deposition rate. The authors believe that during a condensation/evaporation controlled droplet formation, samples with identical thermal properties, but different surface properties would behave closer to a constant wetted area fraction. A constant number of droplets can be approximated when the hygroscopic properties of salts control the electrolyte in the absence of a temperature gradients (space or time).

The corresponding droplet distributions are given in Fig. 7.

2.3. Assumptions

In order to enable the modelling, certain assumptions and simplifications were made throughout the modelling process, in all different aspects. In this section, the assumptions are briefly discussed for each subcomponent.

2.3.1. Single droplet model

In the single droplet model, the electrochemical parameters are assumed to be constant and in standard conditions. The electrochemical kinetic parameters: the open circuit potentials, exchange current densities and transfer coefficients for the half-cell reactions are in reality a function of the droplet size and species concentrations. The main goal of this work is to demonstrate a new approach in corrosion modelling, and therefore the parameters under standard conditions are used.

A second assumption is that the formed corrosion products do not influence the corrosion processes. The corrosion products are thus not included in the model. The output of such a model, can thus be seen as a worst case scenario: the complete wetted surface is available and all oxidation processes affect the metal substrate.

The third assumption is that model is steady-state. Time dependent effects are thus ignored.

2.3.2. Droplet size distributions

As discussed in a previous section, is that a measured droplet size distribution if taken from literature and shifted to higher average droplet radii. When performing these shifts, different assumptions are made dependent on the shift type. When keeping the total number of droplets constant, all droplets are increased by the same (absolute) amount. At a

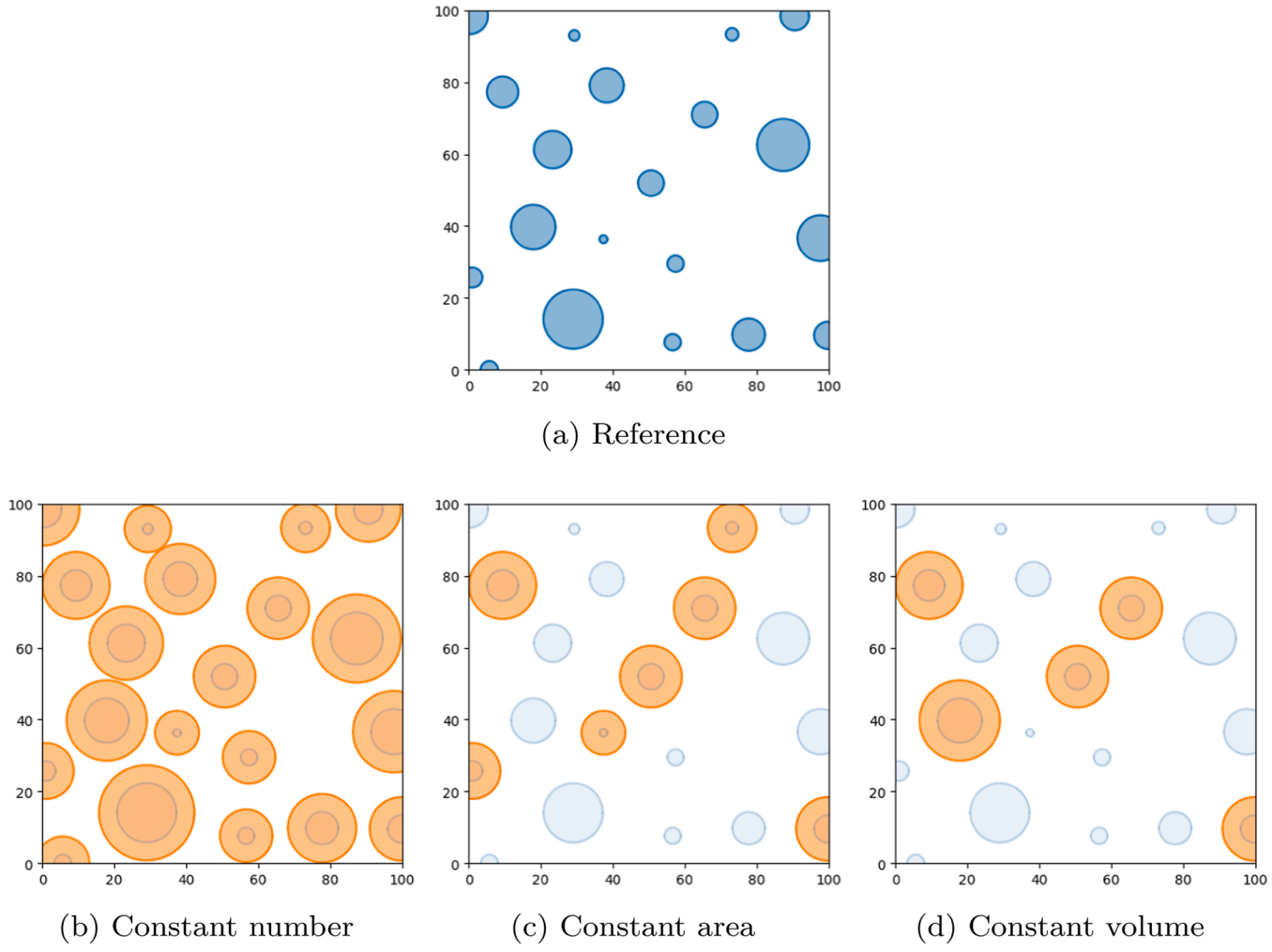

Fig. 6. Illustration of droplet size distribution shifts under different conditions. The blue circles show the original droplets, while the orange circles show the droplets after the distribution shift under the different conditions. These illustrations are purely to demonstrate the different shift conditions and their implications and do not represent the distributions actually used.

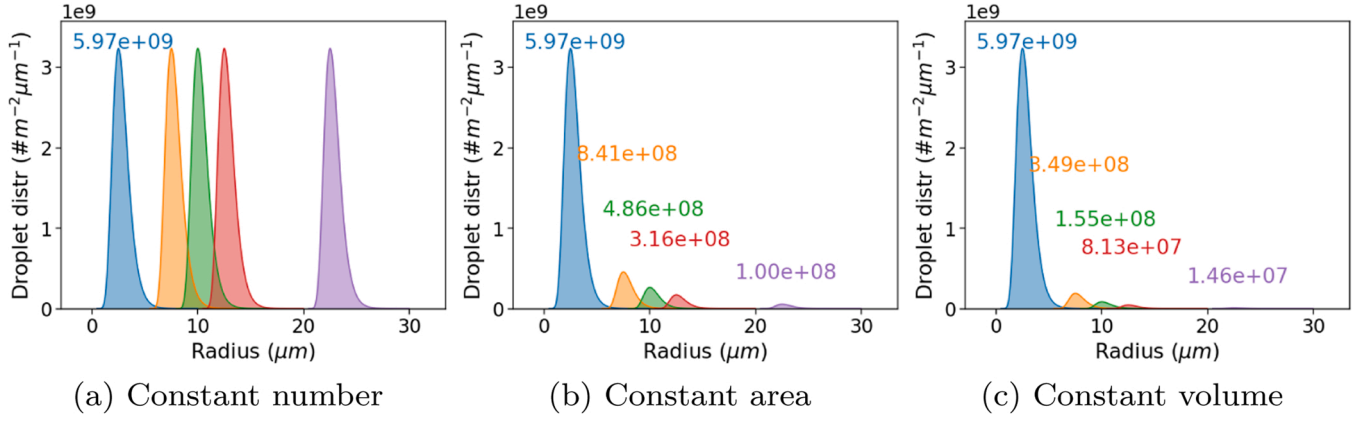

Fig. 7. Droplet distributions under the different constraints. The numbers above the curves are the integrated values over the distribution (total number of droplets).

certain point, the total wetted area surpasses the available area, which is currently ignored. When keeping the contact area or total electrolyte volume constant, the number of droplets per radius are all reduced by the same factor to comply with the imposed conditions.

Furthermore, are the size distributions frozen in time. In reality, droplet (size) distributions constantly change due to condensation, evaporation, gravitational and other effects. These are not considered in the current work.

2.3.3. *Combined*

The previous discussed assumptions will logically affect the combined results. The predicted (yearly) material loss rates assume that the

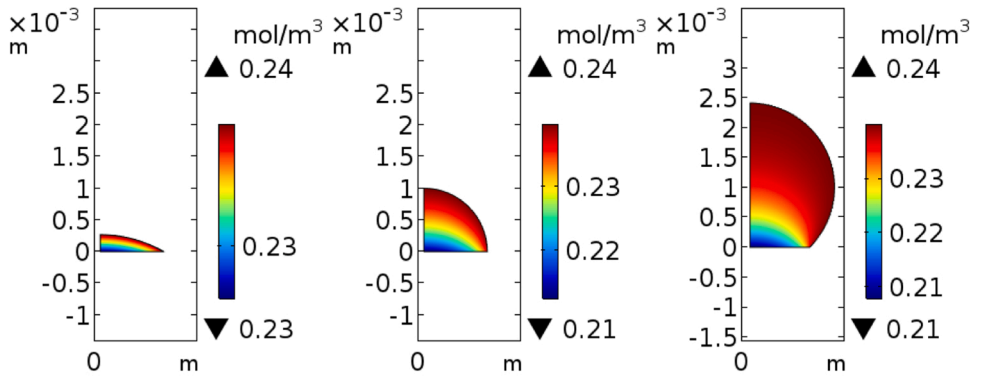

Fig. 8. O_2 concentration profiles for three different contact angles ($\theta = 30^{\circ}$, 90° and 135°) for a wetted radius of 1 mm. The difference in contact angle causes different aeration and thus different oxygen accessibility.

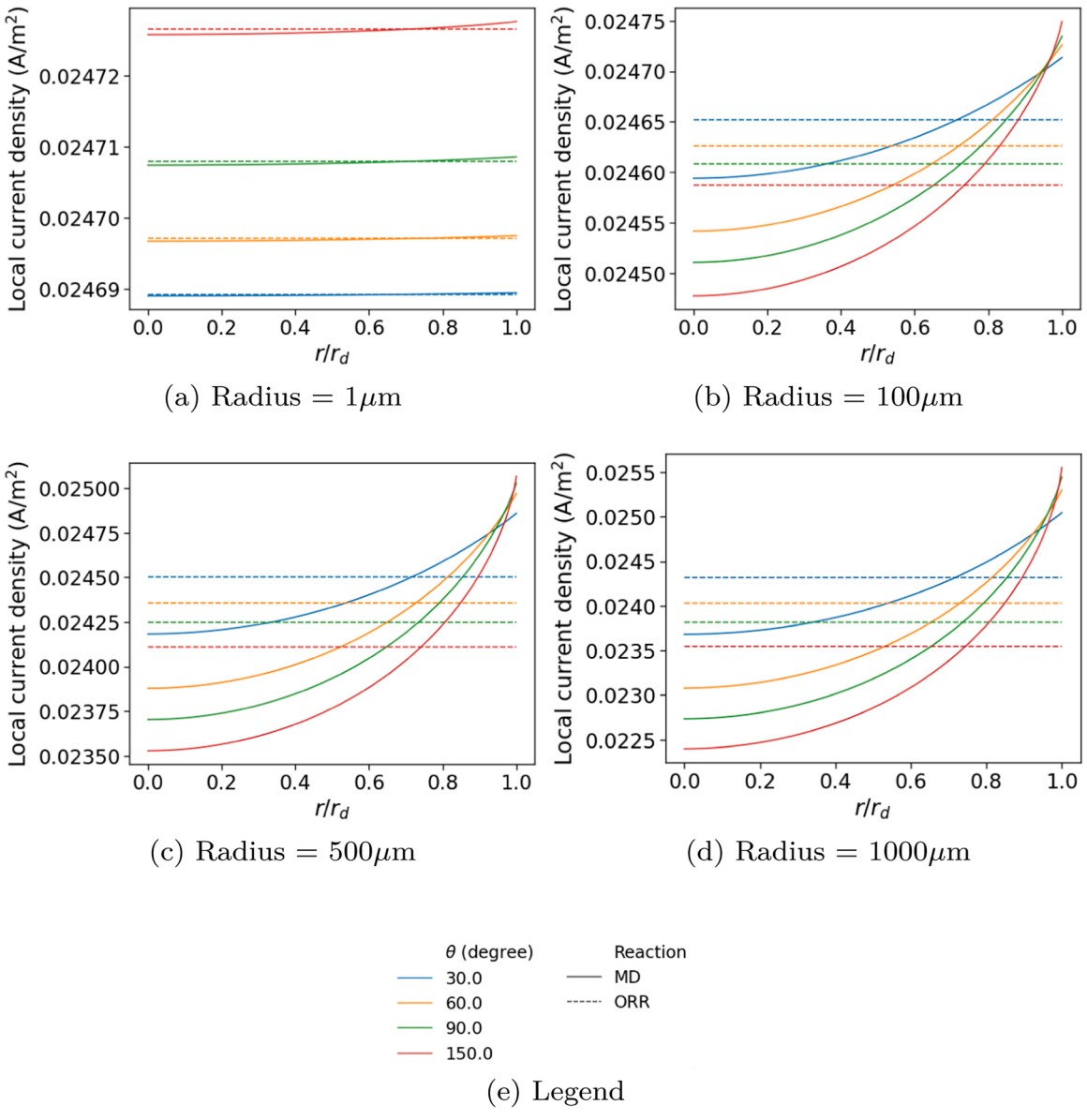

Fig. 9. The absolute current densities as a function of the location for different contact angles for four different droplet radii.

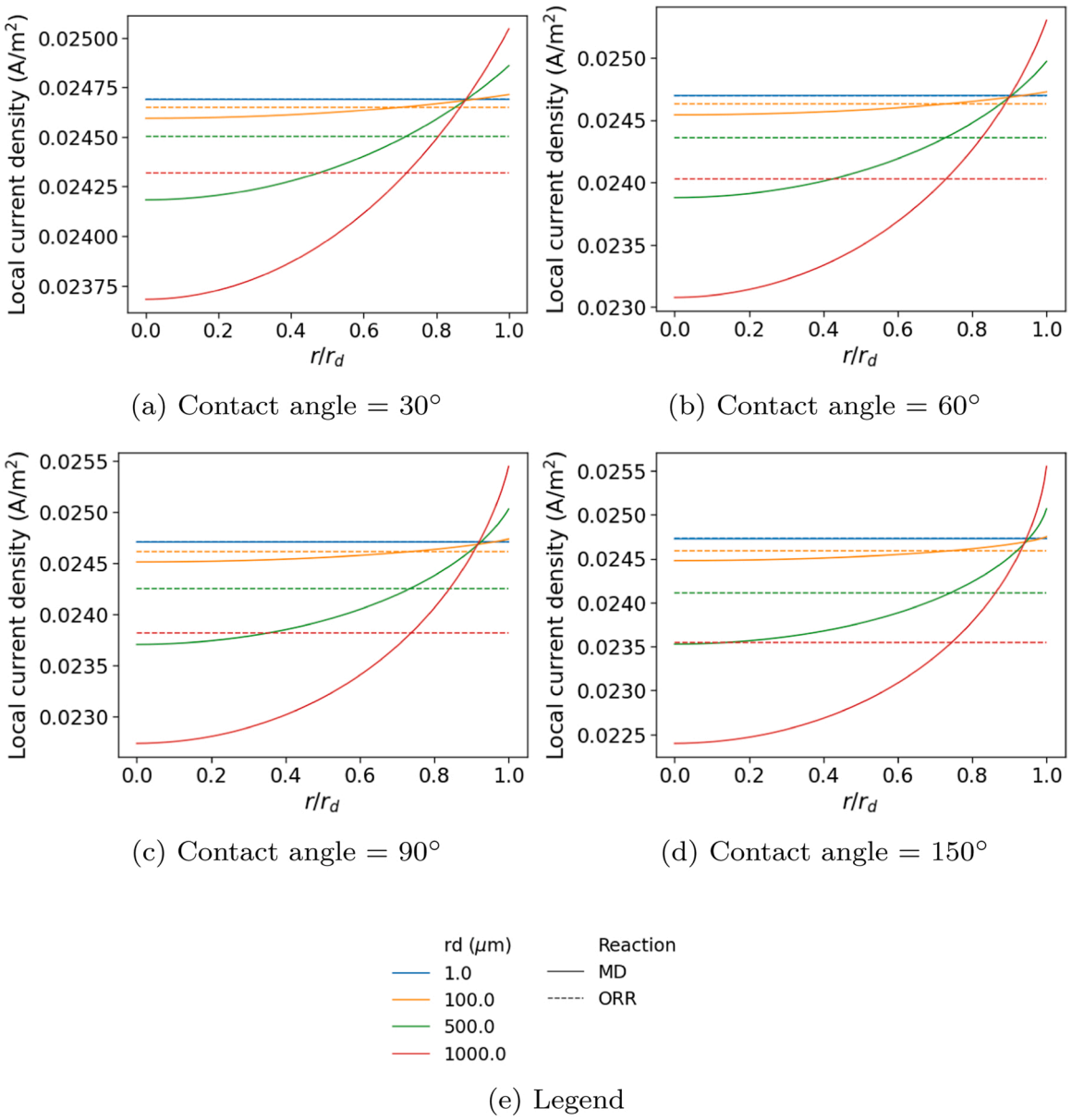

Fig. 10. The absolute current densities as a function of the location for different droplet radii for four different contact angles.

material loss can be averaged over the surface.

3. Results and discussion

3.1. Single droplet

The steady-state single droplet corrosion model provides detailed information about the corrosion processes and the oxygen concentration throughout the given droplet. An example of the computed oxygen concentration profile for three different contact angle values is given in Fig. 8. From these figures, one can immediately observe that the oxygen concentration values at the metal/electrolyte interface are the lowest for the higher contact angle values. In an oxygen diffusion limited regime, this means that the corrosion current density will be lower for the higher contact angles as there is less oxygen available at the interface.

In Figs. 9 and 10 the absolute values of the current densities of the metal dissolution and oxygen reduction are illustrated as a function of the relative position. Fig. 9 illustrates the local current densities for four different contact angles for four different droplet radii. Fig. 10 illustrates

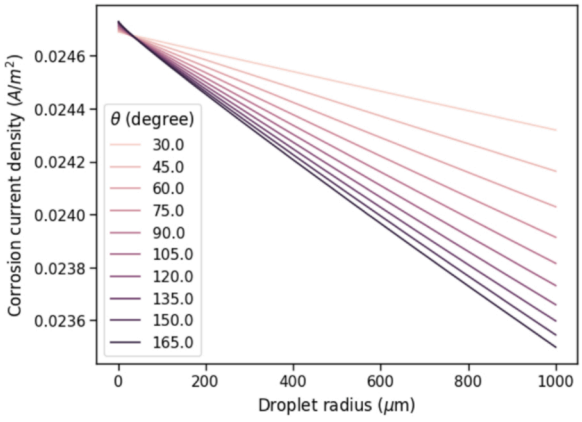

Fig. 11. Averaged corrosion current densities for iron as function of the contact angle and droplet radius.

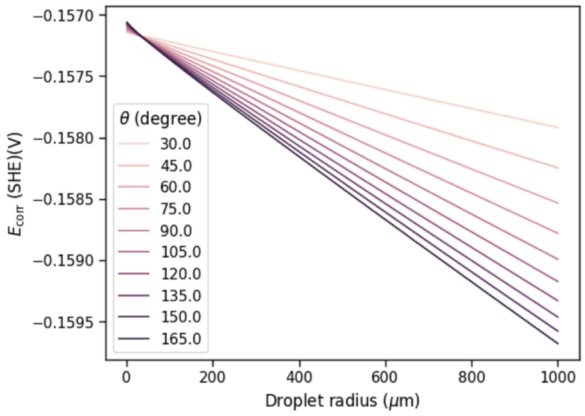

Fig. 12. Corrosion potential on iron as a function of the contact angle and droplet radius.

Table 1
Corrosion parameters on iron [32].

Parameter	Units	Value
n_{MD}	–	2
n_{ORR}	–	2
$i_{0,MD}$	$A\ m^{-2}$	10^{-4}
$i_{0,ORR}$	$A\ m^{-2}$	$4.71e^{-7}$
α_a	–	0.754
α_c	–	0.246
c_{0,O_2}	mol m^{-3}	0.24
$E_{eq,MD}$	V	-0.76
$E_{eq,ORR}$	V	0.401

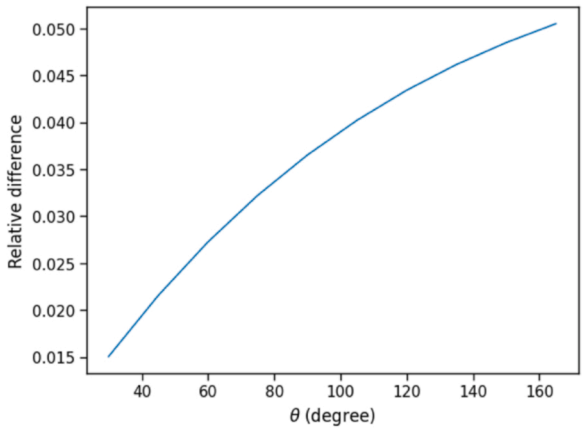

Fig. 13. Relative difference min/max corrosion current densities on iron as a function of the contact angle.

the local current densities for four different droplet radii for four different contact angles.

The metal dissolution current density can be averaged over the surface for different contact angles and droplet radii. The results are shown in Fig. 11 for iron. The resulting corrosion potential are shown in Fig. 12. The used parameters are given in Table 1.

As expected, the current densities increase with decreasing contact radius. The changes are less pronounced for smaller contact angles.

The relative difference between the largest and smallest current densities relative to the average current density as a function of the contact angle is illustrated in Fig. 13. It shows that the relative differences are the smallest for the lowest contact angles. This can easily be explained by the flatter shape of the droplets, causing increased accessibility to oxygen and a higher uniformity in oxygen concentration over the electrode/electrolyte interface.

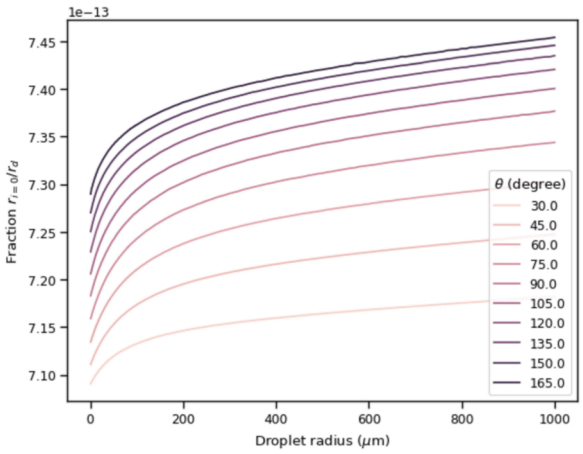

Fig. 14. Relative location where the local current density is zero.

The (relative) location where the total current density is zero on iron as a function of the average droplet radius and contact angle is illustrated in Fig. 14. This is the relative location when it changes from net anode to net cathode. With increasing contact radius and increasing contact angle the (relative) position moves away from the centre.

3.2. Droplet distribution

The averaged single droplet corrosion current densities (Fig. 11) can be combined with the droplet size distributions (Fig. 7). This methodology allows combining (detailed) finite element single droplet corrosion results with (imposed) droplet size distributions. As already mentioned above, both the single droplet corrosion and the droplet size distributions are time dependent. Moreover, both are strongly coupled phenomena. The time depended behaviour is not directly included in the presented work. The results in this work, could be considered as snapshots in time, to illustrate the current densities and corrosion rates at the current conditions.

These size distributions correspond to the following corrosion current density distributions are shown in Fig. 15. Depending on the corresponding shift, the corrosion rate can differ rather drastically. When the number of droplets is kept constant for the different distributions, the current density increases rapidly from 0.00406 A m^{-2} to 0.24209 A m^{-2}. As expected, the differences for constant area are limited, as the selected range of droplet sizes is limited. With constant electrolyte volume, a rapid decrease in current density is predicted (from 0.00406 A m^{-2} to 0.00059 A m^{-2}). The averaged corrosion current densities within the droplet radii range considered in the distributions in this section are shown in Fig. 16. It can be observed that the maximal difference in this zone is less than $6e^{-5}$ A/m^2 for iron. The relative change in total corrosion current as a function of the relative increase in average droplet radius can be fitted to a power-law of the form

$$\frac{i}{i_0} = a\left(\frac{r}{r_0}\right)^k. \tag{6}$$

In this relation, $\frac{i}{i_0}$ is the (total) current density (i) compared to the reference current density (i_0), a and k are fitted constants. In Fig. 17 the log-log relation is plotted in combination with the fitted curves, with the fitted parameters added in the figure. The power law fitting demonstrates the strong dependency of the corrosion current density on the average droplet radius depending on the imposed electrolyte conditions. It illustrates that the droplet distribution is critical information needed to make accurate predictions. When the number of droplets is constant, the corrosion current density increases exponentially with increasing droplet size. On the other hand, if the electrolyte volume is constant, the

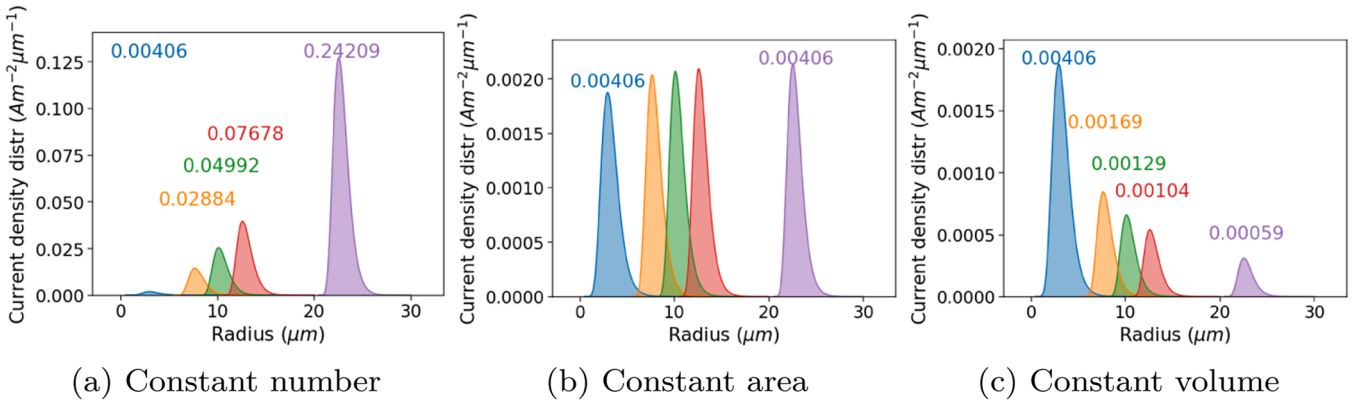

Fig. 15. Droplet corrosion current distributions under the different constraints on iron. The corrosion current density contribution by each droplet size is indicated for each distribution under the different shift conditions. The current densities given in A/m^2 of the complete distributions are indicated above the bell curves.

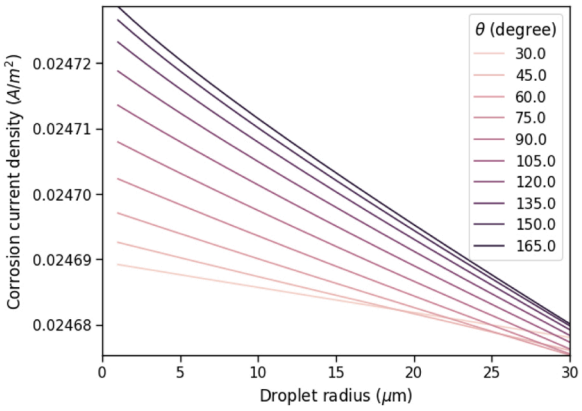

Fig. 16. Averaged corrosion current densities on iron as function of the radii relevant for the used size distributions.

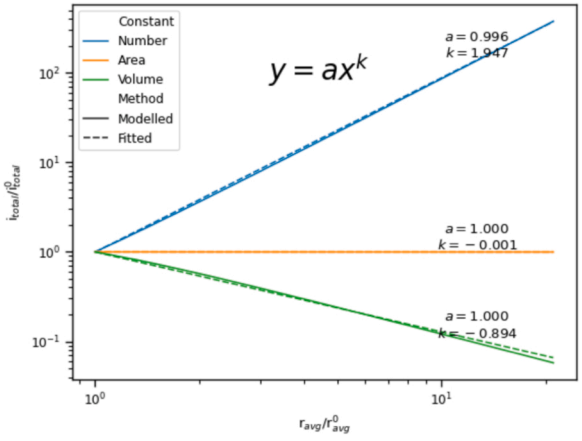

Fig. 17. Comparison of the corrosion current density change as function of the average droplet radius.

current density will decrease slower and slower as the average radius increases.

From the observed differences in Fig. 15 it is clear that for this type of distributions with a limited range of the droplet sizes (between 1 and 30 μm), the covered/wetted area is the critical parameter, as plotted in Fig. 18. The wetted area is thus identified as the key parameter, at least for small droplets. Increasing the contact angle while keeping the total volume of electrolyte constant results in a drastic reduction of the total

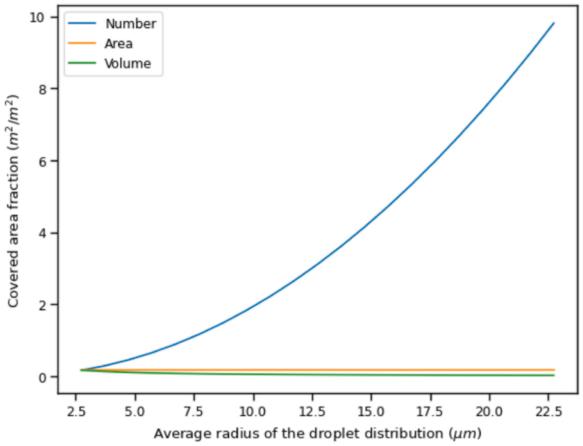

Fig. 18. Area fraction covered/wetted by the droplet distributions as a function of the radii. Moving the distribution to larger sizes while keeping the number of droplets constant is not physically possible, as the covered area is higher than the available area.

material loss. Increasing the contact angle would reduce the runoff droplet size.

3.3. Corrosion depths

The current distributions can be translated to expected surface averaged corrosion depth rates using Faraday's law (Fig. 19 for iron).

From these results, it is clear that the covered area plays a key role, and not necessarily the total volume of the electrolyte.

The calculated thickness losses after one year are shown in Fig. 20. The ISO standard [39] defines six different corrosivity categories based on the yearly material loss for different materials. These relevant categories are indicated on the figures. It is important to stress the assumption that a fixed droplet size distribution is present at the surface during the complete period and that the corrosion products do not influence the corrosion rates. In a real outdoor exposure test, the time of wetness could be much lower than 100%, strongly reducing the corrosion depth. Furthermore, the droplet size distribution will evolve over time in outdoor conditions and could reach average radii well into the millimetre range, resulting in different corrosion current densities (Fig. 11).

The droplet size distributions can have close to a factor of 7 impact on the actual corrosion rate observed for the same electrolyte volume when the average radius is shifted from 2.7 μm to 22.7 μm. This significant increase could explain the differences reported in literature

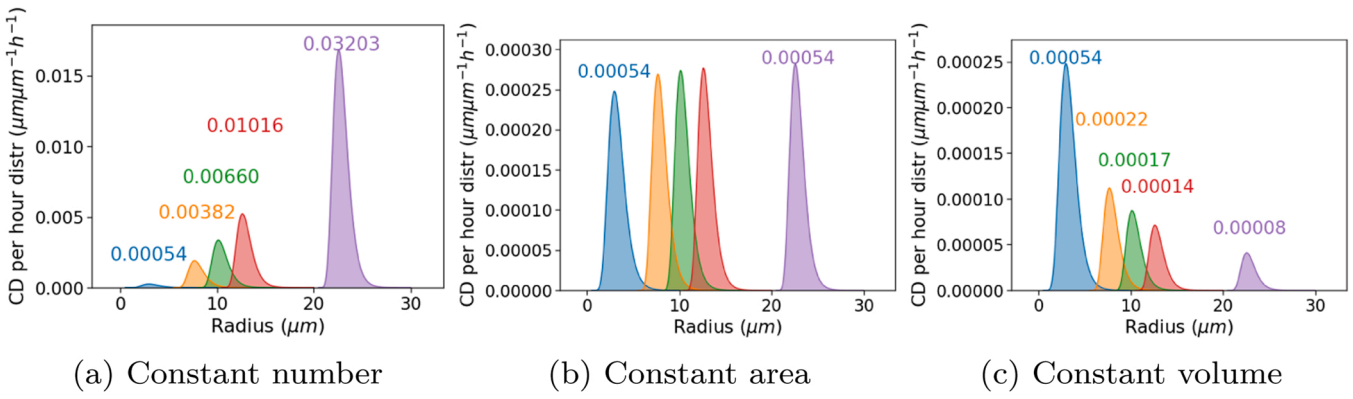

Fig. 19. Corrosion rate for different distributions on iron. The integrated (total) corrosion rate is indicated above in µm/h.

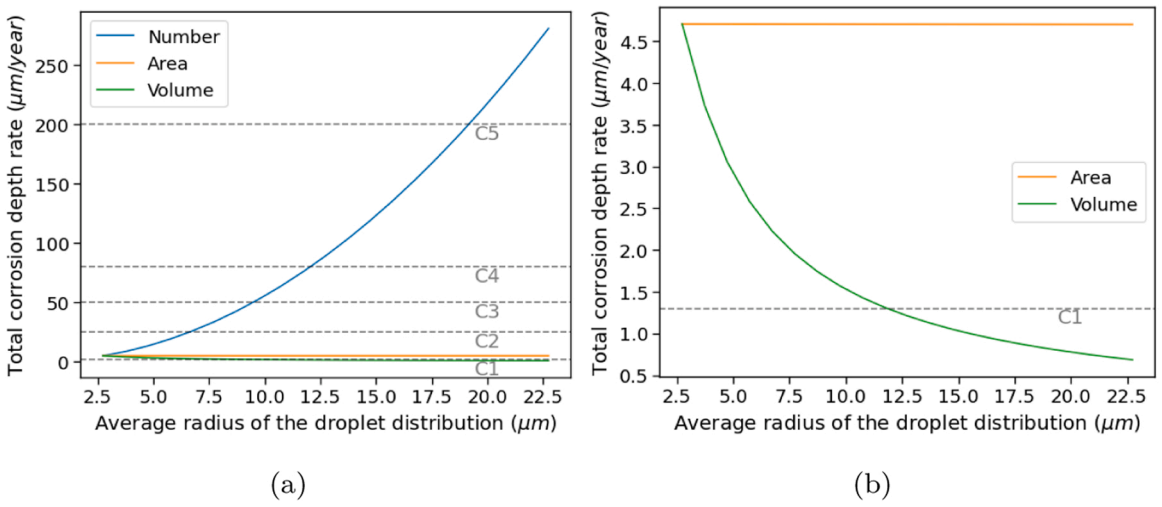

Fig. 20. Thickness loss rate on iron as a function of the average droplet distribution radius under different conditions over the surface.

between tests in experimental investigations. The approach detailed in this work could help explain these difference in combination with experimental data on the droplet size and geometry distribution. Increased knowledge could then possibly resulting in more reproducible and representative accelerated tests, providing a clearer link with outdoor exposure tests and in-service performance.

The main limitation of the discussed model is the steady state nature of the single droplet model, therefore the presented results are not suited to predict long-term losses. From the moment on when corrosion products are formed, the corrosion kinetics and wetting behaviour deviate from the implemented values. Adding time dependency, including the effect of corrosion product formation is desired, but adds a high amount of complexity.

4. Conclusion

In this work, a new approach is proposed to evaluate and quantify the importance of droplet (size) distributions with relation to atmospheric corrosion. With this methodology, detailed finite element single droplet corrosion modelling results are combined with (assumed) droplet size distributions.

A steady-state iron corrosion model, including oxygen reduction reaction and metal dissolution was computed for single droplets with different droplet radii and contact angles. The predicted corrosion current densities were then combined with different proposed (shifted) droplet size distributions. The distributions were shifted presuming three different conditions: constant number of droplets, constant wetted area and constant electrolyte volume.

The corrosion rate differences when comparing different droplet sizes individually are rather small, but for a collection of droplets over a surface, this could have a major impact on the (surface) averaged corrosion rate. The obtained corrosion loss predictions show a strong dependence on the droplet size distribution as a difference up to a factor of 7 was observed when comparing the considered extremes. Under certain conditions, with the correct input parameters, significant differences could be observed. The availability of the presented model create an incentive to increase the monitoring efforts of the electrolyte during accelerated corrosion and other corrosion experiments.

In its current base state of complexity, the proposed model can be applied to experimental observations in order to understand the differences between different accelerated corrosion tests and experiments. The next step therefore consists of introducing relevant experimental data obtained during accelerated corrosion tests.

CRediT authorship contribution statement

N. Van den Steen: Conceptualization, Writing – original draft. **Y. Gonzalez-Garcia:** Conceptualization, Writing – review & editing. **J.M.C Mol:** Conceptualization, Writing – review & editing. **H. Terryn:** Supervision, Conceptualization, Writing – review & editing. **Y. Van Ingelgem:** Supervision, Conceptualization, Writing – review & editing.

Declaration of Competing Interest

The authors declare that they have no known competing financial interests or personal relationships that could have appeared to influence the work reported in this paper.

Data availability

The raw data required to reproduce these findings cannot be shared at this time due to technical or time limitations. The processed data required to reproduce these findings cannot be shared at this time due to technical or time limitations.

Acknowledgements

This research was carried out under Project no. T18016 in the framework of the Research Program of the Materials innovation institute (M2i) (www.m2i.nl) supported by the Dutch government.

References

[1] T. Prosek, N.L. Bozec, D. Thierry, Application of automated corrosion sensors for monitoring the rate of corrosion during accelerated corrosion tests, Mater. Corros. 65 (2012) 448–456, https://doi.org/10.1002/maco.201206655.
[2] P. Montoya, I. Díaz, N. Granizo, D. de la Fuente, M. Morcillo, An study on accelerated corrosion testing of weathering steel, Mater. Chem. Phys. 142 (2013) 220–228, https://doi.org/10.1016/j.matchemphys.2013.07.009.
[3] N. LeBozec, D. Thierry, A. Peltola, L. Luxem, G. Luckeneder, G. Marchiaro, M. Rohwerder, Corrosion performance of Zn-Mg-Al coated steel in accelerated corrosion tests used in the automotive industry and field exposures, Mater. Corros. 64 (2013) 969–978, https://doi.org/10.1002/maco.201206959.
[4] N. LeBozec, D. Thierry, P.L. Calvé, C. Favennec, J.-P. Pautasso, C. Hubert, Performance of marine and offshore paint systems: correlation of accelerated corrosion tests and field exposure on operating ships, Mater. Corros. 66 (2013) 215–225, https://doi.org/10.1002/maco.201307340.
[5] M.S. Azevedo, C. Allély, K. Ogle, P. Volovitch, Corrosion mechanisms of zn(mg, al) coated steel in accelerated tests and natural exposure: 1. The role of electrolyte composition in the nature of corrosion products and relative corrosion rate, Corros. Sci. 90 (2015) 472–481, https://doi.org/10.1016/j.corsci.2014.05.014.
[6] N. LeBozec, N. Blandin, D. Thierry, Accelerated corrosion tests in the automotive industry: a comparison of the performance towards cosmetic corrosion, Mater. Corros. 59 (2008) 889–894, https://doi.org/10.1002/maco.200804168.
[7] M. Stratmann, H. Streckel, K.T. Kim, S. Crockett, On the atmospheric corrosion of metals which are covered with thin electrolyte layers–iii. The measurement of polarisation curves on metal surfaces which are covered by thin electrolyte layers, Corros. Sci. 30 (1990) 715–734, https://doi.org/10.1016/0010-938x(90)90034-3.
[8] J. Weissenrieder, C. Leygraf, In situ studies of filiform corrosion of iron, J. Electrochem. Soc. 151 (2004) B165, https://doi.org/10.1149/1.1645263.
[9] Z. Liu, W. Wang, J. Wang, X. Peng, Y. Wang, P. Zhang, H. Wang, C. Gao, Study of corrosion behavior of carbon steel under seawater film using the wire beam electrode method, Corros. Sci. 80 (2014) 523–527, https://doi.org/10.1016/j.corsci.2013.11.012.
[10] J.-H. Ahn, Y.-S. Jeong, I.-T. Kim, S.-H. Jeon, C.-H. Park, A method for estimating time-dependent corrosion depth of carbon and weathering steel using an atmospheric corrosion monitor sensor, Sensors 19 (2019) 1416, https://doi.org/10.3390/s19061416.
[11] S. Wan, J. Hou, Z.-F. Zhang, X. Zhang, Z.-H. Dong, Monitoring of atmospheric corrosion and dewing process by interlacing copper electrode sensor, Corros. Sci. 150 (2019) 246–257, https://doi.org/10.1016/j.corsci.2019.02.008.
[12] I.S. Cole, D.A. Paterson, Mathematical models of dependence of surface temperatures of exposed metal plates on environmental parameters, Corros. Eng., Sci. Technol. 41 (2006) 67–76, https://doi.org/10.1179/174327806×94045.
[13] N. Van den Steen, H. Simillion, O. Dolgikh, H. Terryn, J. Deconinck, An integrated modeling approach for atmospheric corrosion in presence of a varying electrolyte film, Electrochim. Acta 187 (2016) 714–723, https://doi.org/10.1016/j.electacta.2015.11.010.
[14] N. Van den Steen, H. Simillion, D. Thierry, H. Terryn, J. Deconinck, Comparing modeled and experimental accelerated corrosion tests on steel, J. Electrochem. Soc. 164 (2017) C554–C562, https://doi.org/10.1149/2.0951709jes.
[15] R.M. Katona, J.C. Carpenter, A.W. Knight, R.S. Marshall, B.L. Nation, E. J. Schindelholz, R.F. Schaller, R.G. Kelly, Editors' choice–convection boundary layer thickness at elevated chloride concentrations and temperatures and the effects on a galvanic couple, J. Electrochem. Soc. 168 (2021), 031512, https://doi.org/10.1149/1945-7111/abeb29.
[16] M.E. Parker, R.G. Kelly, Improved atmospheric corrosion testing for aluminum alloys, Part i: deconstructing ASTM G85-A2, Corrosion 76 (2020) 39–50.
[17] F.F. Chen, M. Breedon, E.D. Sapper, W. Ganther, D. Lau, I. Cole, A microclimate model to simulate neutral salt spray testing for corrosion inhibitor evaluation and functional coating development, Prog. Org. Coat. 111 (2017) 327–335, https://doi.org/10.1016/j.porgcoat.2017.06.010.
[18] I.S. Cole, W.D. Ganther, J.D. Sinclair, D. Lau, D.A. Paterson, A study of the wetting of metal surfaces in order to understand the processes controlling atmospheric corrosion, J. Electrochem. Soc. 151 (2004) B627, https://doi.org/10.1149/1.1809596.
[19] I.S. Cole, D. Lau, D.A. Paterson, Holistic model for atmospheric corrosion Part 6 - from wet aerosol to salt deposit, Corros. Eng. Sci. Technol. 39 (2004) 209–218, https://doi.org/10.1179/147842204X2880.
[20] I.S. Cole, D.A. Paterson, Holistic model for atmospheric corrosion Part 7 – cleaning of salt from metal surfaces, Corros. Eng. Sci. Technol. 42 (2007) 106–111, https://doi.org/10.1179/174327807X196807.
[21] C.M. Hangarter, S.A. Policastro, Electrochemical characterization of galvanic couples under saline droplets in a simulated atmospheric environment, Corrosion 73 (2016) 268–280, https://doi.org/10.5006/2254.
[22] T. Tsuru, K.-I. Tamiya, A. Nishikata, Formation and growth of micro-droplets during the initial stage of atmospheric corrosion, Electrochim. Acta 49 (2004) 2709–2715, https://doi.org/10.1016/j.electacta.2004.01.032.
[23] G. El-Mahdy, H.A. Al-Lohedan, Z. Issa, Monitoring the corrosion rate of carbon steel under a single droplet of NaCl, Int. J. Electrochem. Sci. 9 (2014) 7977–7985.
[24] S.Y. Misyura, The dependence of drop evaporation rate and wettability on corrosion kinetics, Colloids Surf. A: Physicochem. Eng. Asp. 610 (2021), 125735, https://doi.org/10.1016/j.colsurfa.2020.125735.
[25] N.S. Azmat, K.D. Ralston, B.C. Muddle, I.S. Cole, Corrosion of Zn under acidified marine droplets, Corros. Sci. 53 (2011) 1604–1615, https://doi.org/10.1016/j.corsci.2011.01.044.
[26] T.H. Muster, A. Bradbury, A. Trinchi, I.S. Cole, T. Markley, D. Lau, S. Dligatch, A. Bendavid, P. Martin, The atmospheric corrosion of zinc: the effects of salt concentration, droplet size and droplet shape, Electrochim. Acta 56 (2011) 1866–1873, https://doi.org/10.1016/j.electacta.2010.09.099.
[27] Y. Wang, W. Wang, Y. Liu, L. Zhong, J. Wang, Study of localized corrosion of 304 stainless steel under chloride solution droplets using the wire beam electrode, Corros. Sci. 53 (2011) 2963–2968, https://doi.org/10.1016/j.corsci.2011.05.051.
[28] S. Li, L.H. Hihara, Atmospheric-corrosion electrochemistry of NaCl droplets on carbon steel, J. Electrochem. Soc. 159 (2012) C461–C468, https://doi.org/10.1149/2.035211jes.
[29] X. Tang, C. Ma, X. Zhou, X. Lyu, Q. Li, Y. Li, Atmospheric corrosion local electrochemical response to a dynamic saline droplet on pure iron, Electrochem. Commun. 101 (2019) 28–34, https://doi.org/10.1016/j.elecom.2019.01.011.
[30] E. Schindelholz, B.E. Risteen, R.G. Kelly, Effect of relative humidity on corrosion of steel under sea salt aerosol proxies, J. Electrochem. Soc. 161 (2014) C450–C459, https://doi.org/10.1149/2.0221410jes.
[31] M.S. Venkatraman, I.S. Cole, D.R. Gunasegaram, B. Emmanuel, Modeling corrosion of a metal under an aerosol droplet, Mater. Sci. Forum 654–656 (2010) 1650–1653, https://doi.org/10.4028/www.scientific.net/msf.654-656.1650.
[32] M.S. Venkatraman, I.S. Cole, B. Emmanuel, Model for corrosion of metals covered with thin electrolyte layers: pseudo-steady state diffusion of oxygen, Electrochim. Acta 56 (2011) 7171–7179, https://doi.org/10.1016/j.electacta.2011.05.009.
[33] B.G. Koushik, Nils Van den Steen, M.H. Mamme, Y.V. Ingelgem, H. Terryn, Review on modelling of corrosion under droplet electrolyte for predicting atmospheric corrosion rate, J. Mater. Sci. Technol. 62 (2021) 254–267, https://doi.org/10.1016/j.jmst.2020.04.061.
[34] R. Leach, F. Stevens, S. Langford, J. Dickinson, Dropwise condensation: experiments and simulations of nucleation and growth of water drops in a cooling system, Langmuir 22 (2006) 8864–8872.
[35] Y.-J. Sheng, S. Jiang, H.-K. Tsao, Effects of geometrical characteristics of surface roughness on droplet wetting, J. Chem. Phys. 127 (2007), 234704, https://doi.org/10.1063/1.2804425.
[36] F. Thébault, B. Vuillemin, R. Oltra, K. Ogle, C. Allely, Investigation of self-healing mechanism on galvanized steels cut edges by coupling SVET and numerical modeling, Electrochim. Acta 53 (2008) 5226–5234, https://doi.org/10.1016/j.electacta.2008.02.066.
[37] D. Fritter, C.M. Knobler, D.A. Beysens, Experiments and simulation of the growth of droplets on a surface (breath figures), Phys. Rev. A 43 (1991) 2858–2869, https://doi.org/10.1103/physreva.43.2858.
[38] T. Song, Z. Lan, X. Ma, T. Bai, Molecular clustering physical model of steam condensation and the experimental study on the initial droplet size distribution, Int. J. Therm. Sci. 48 (2009) 2228–2236, https://doi.org/10.1016/j.ijthermalsci.2009.05.004.
[39] E. ISO 9223, Corrosion of Metals and Alloys-corrosivity of Atmospheres–Classification, Determination and Estimation, The British Standard Institute, 2012.